Three-Dimensional, Shock-on-Shock Interaction Problem

Paul Kutler* and Leonidas Sakell†

NASA Ames Research Center, Moffett Field, Calif.

The unsteady, three-dimensional flowfield resulting from the interaction of a plane shock with a cone-shaped vehicle traveling supersonically is determined using a second-order, shock-capturing, finite-difference approach. The time-dependent, inviscid gas dynamic equations are transformed to include the self-similar property of the flow, to align various coordinate surfaces with known shock waves, and to cluster points in the vicinity of the intersection of the transmitted incident shock and the surface of the vehicle. The governing partial differential equations in conservation-law form are then solved iteratively using MacCormack's algorithm. The computer simulation of this problem, compared with its experimental counterpart, is relatively easy to model and results in a complete description of the flowfield including the peak surface pressure. The numerical solution, with its complicated wave structure, compares favorably with the available schlieren photographs, and the predicted peak surface pressures obtained are shown to agree better with the experimental data than existing approximate theories.

I. Introduction

FOR over a decade, experimentalists and theoreticians have studied the flowfield generated by the interaction of an incident shock wave (e.g., that generated by a nuclear explosion from an offensive re-entry vehicle or by a sister craft [fratricide]) with a vehicle traveling at supersonic speeds (see Fig. 1a). In the past, a great deal of attention focused on determining the strong-blast-induced transient pulse produced at the surface of the vehicle because of the belief that the forces generated might be structurally damaging. Recently, however, a new question has emerged concerning weak incident shocks $(p_3/p_1 < 2)$; i.e., can such an encounter induce high-frequency disturbances capable of destroying the internal structure or appended equipment? The purpose of this paper is to compute the flowfield generated by such an encounter, and thus predict the resulting transient surface pressures required by the designer to determine the structural and vibrational responses of the vehicle.

A typical flowfield resulting from the interaction of a planar shock at Mach number M_i and inclination λ, and a pointed cone with half-angle σ at Mach number M_v and angle-of attack α is shown in Fig. 1b. It consists of a multitude of shock waves and slip surfaces, which interact to yield a rather complicated three-dimensional, unsteady flowfield. Since the velocity vector of the conical vehicle and the impinging shock are assumed to be coplanar, the flowfield is symmetric with respect to this plane. To the right of the incident shock, there exists a conical flow generated by the vehicle in the freestream
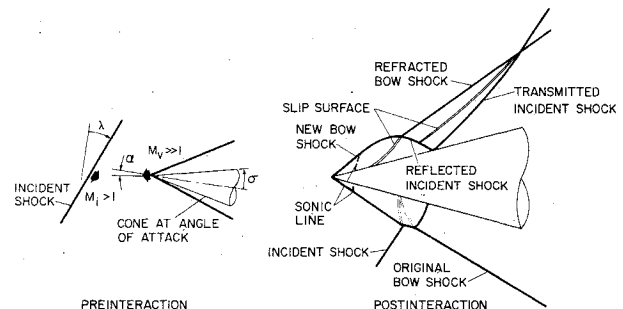
Fig. 1 Preinteraction and postinteraction wave patterns for the three-dimensional shock-on-shock problem.

or preblast conditions, while to the left of the indicated sonic line there exists a second conical flow generated by the body traveling in the post-blast environment. Both conical-flow solutions can be generated from existing three-dimensional, supersonic, steady-flow computer codes. The region between these two flows, which contains the intricate shock structure, is the crux of the present problem and is determined here.

The region of the shock-on-shock flowfield of most interest to the vehicle designer is where the transmitted incident shock strikes the body, for it is the circumferential variation of the flow variables behind this impingement line that can generate the undesirable forces. The transmitted shock at the body depending on its inclination, can transit from a Mach reflection on the lower surface or leeward side to a regular reflection on the top surface or windward side, or result in a Mach reflection entirely around the body. Most of the interest and recent experimental testing centers around the incident shock, inclination angle that yields transition from regular to Mach reflection in the windward plane. This encounter angle is believed to result in the largest or "peak" surface pressure. Therefore, only values of the incident shock inclination near transition are considered here; thus such possibilities as the broadside encounter are ruled out.

In the past, there have been numerous theoretical attempts[1-9] to obtain solutions for the three-dimensional, shock-on-shock (TDSOS) problem, some of which have resulted in computer programs.[6,9-14] This paper does not try to summarize them by commenting on the relative merits or shortcomings of each, rather the reader is referred to papers

by Aiello,[15] and Kutler et al.[9] for brief summaries of some of the existing theories. In general, most of the early theories required assumptions regarding the position and structure of the existing shock waves for their model. Consequently, an incorrect assumption of the shock structure could invalidate the resulting theory. A big disadvantage of the approximate techniques that exist today for solving the TDSOS problem is that, in most of them, both the radial and circumferential gradients of the flowfield are neglected. These gradients affect the position and inclination of the transmitted incident shock as it strikes the body and can therefore gravely affect shock transition and the predicted peak surface pressure. In fact, compared with available experimental data, all of the approximate theories overpredict the peak pressure. This comparison generated concern from the missile-maker and led to a rather exhaustive and expensive experimental study.

There have been many experimental investigations[16-22] of the TDSOS problem in the past, resulting in some very good schlieren photographs of the interactive shock structure and surface pressure distributions. The most recent experimental testing[23,24] was performed at Holloman Air Force Base by using a rocket-propelled sled. The earlier studies involved relatively strong incident shocks, while the latest tests dealt mainly with the weaker blast waves because of their greater probability of occurrence. The numberical results presented later are compared with both the earlier and most recent experimental data.

The approach used here to solve the TDSOS problem parallels that of the two-dimensional procedure[9] in which the shock-capturing technique (SCT) was employed. The self-similarity of the problem, which results from the absence of a characteristic length associated with the planar incident shock or the vehicle itself, is used to transform the three-dimensional unsteady problem to an equivalent steady-flow problem. The resulting set of partial differential equations is of mixed elliptic-hyperbolic type, but is made totally hyperbolic by reintroducing the unsteady term. With correct application of the appropriate boundary conditions, the governing equations can be solved iteratively as a mixed initial boundary value problem using existing explicit, finite-difference algorithms.

The TDSOS procedure developed here properly accounts for both the radial and circumferential gradients generated by the conical-flow solutions, and results in a complete description of the entire flowfield, including the shock structure and surface pressure distribution. Unlike the experimental counter-part, a typical numerical solution is quite inexpensive and requires approximately 18 min of CDC 7600 computer time.

II. Governing Equations

In extending the two-dimensional problem[9] to three dimensions, a cylindrical coordinate system (t, z, r, ϕ) is selected with the origin located at the vertex of the cone, and ϕ measured from the lower plane of symmetry (see Fig. 2). The inclination λ of the incident shock is measured with respect to a plane perpendicular to the axis of the cone. In following the idea of aligning the coordinates with the position of known shock waves[9,25] to reduce the postcursor and precursor oscillations associated with the shock-capturing technique, an independent variable transformation is performed. The longitudinal coordinate z is transformed $\zeta = \zeta \, (t, z, r, \phi)$ so that the resulting constant ζ planes are parallel to and moving in the direction of the planar incident shock, while the radial coordinate r is transformed $\eta = \eta \, (t, z, r, \phi)$ to normalize the distance between the body and an outer boundary. The outer boundary is chosen so that in the two regions of known conical flow, namely, near the right- and left-hand end planes, it is a conical surface. Between these two regions, and in each meridional plane, the outer boundary is composed of a cubic polynomial that approximately parallels the peripheral shock. In addition to the shock-alignment trans-
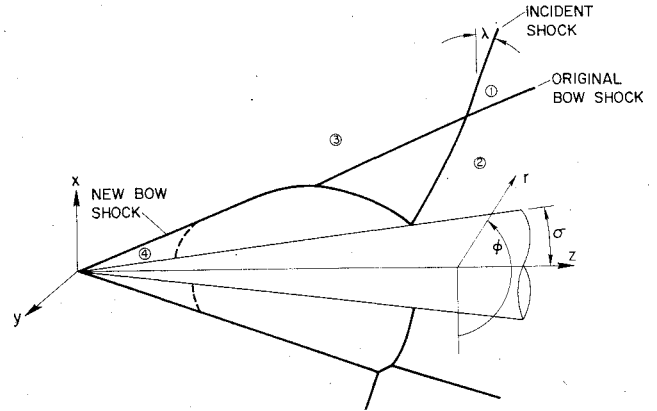

Fig. 2   Coordinate system.

formations, the new logitudinal coordinate ζ is again transformed $\mu = \mu \, (\zeta)$ to cluster points[26] near the impingement point on the body of the transmitted incident shock, since the flow in this region is of paramount importance. Thus, including the self-similar property of the flow, the resulting independent variable transformation from (t, z, r, ϕ) to (t, μ, η, ξ) space is

$$\tau = t, \quad \eta = \frac{r - r_b(z)}{r_{ob}(t, z, \phi) - r_b(z)}, \quad \xi = \phi$$

$$\mu = \begin{cases} \zeta_{max} \{ C + (1/\beta) \sinh^{-1} [(\zeta/\zeta_c) - 1] \sinh \beta C \} & \beta > 0 \\ \\ \zeta & \beta = 0 \end{cases}$$

(1)

where

ζ	$= [z - z_{pl}(t, r, \phi)]/t$
C	$= 1/(2\beta) \ell n \{ [1 + (e^\beta - 1) \zeta_c/\zeta_{max}]$ $/ [1 - (1 - e^{-\beta}) \zeta_c/\zeta_{max}] \}$
$z_{pl}(t, r, \phi)$	$= \dot{z}_m t - r \cos \phi \tan \lambda$ (equation of planes parallel to incident shock)
λ	$=$ incident shock inclination (see Fig. 2)
$\dot{z}_m$	$=$ velocity of left-hand boundary of computational volume $= z_{min}/t$ [see Eq. (5)]
ζ_c	$=$ value of ζ about which points are to be clustered
ζ_{max}	$=$ maximum value of ζ
β	$=$ clustering parameter; concentration of points increases with β
$r_b(z)$	$= z \tan \sigma$ (equation of the body)
σ	$=$ cone half-angle
$r_{ob}(t, z, \phi)$	$=$ equation of the outer boundary (discussed in the Sect. III)

Applying this transformation to the three-dimensional, time-dependent Euler equations yields the following partial differential equation in conservation-law form

$$U_\tau + E_\mu + F_\eta + G_\xi + H = 0 \quad (2)$$

where

$U = U^*$

$E = \mu_\zeta (\zeta_t U^* + \zeta_z E^* + \zeta_r F^* + \zeta_\phi G^*)$

$F = \eta_t U^* + \eta_z E^* + \eta_r F^* + \eta_\phi G^*$

$G = G^*$

$H = H^* - U^* (\zeta_{t\zeta} + \mu_{\zeta_\mu} \zeta_t + \eta_{t\eta}) - E^* (\zeta_{z\zeta} + \mu_{\zeta_\mu} \zeta_z + \eta_{z\eta})$

$\quad - F^* (\zeta_{r\zeta} + \mu_{\zeta_\mu} \zeta_r + \eta_{r\eta}) - G^* (\zeta_{\phi\zeta} + \mu_{\zeta_\mu} \zeta_\phi + \eta_{\phi_\eta})$

and

$$U^* = \begin{bmatrix} \rho \\ \rho u \\ \rho v \\ \rho w \\ e \end{bmatrix}, E^* = \begin{bmatrix} \rho u \\ p + \rho u^2 \\ \rho u v \\ \rho u w \\ (e+p)u \end{bmatrix}, F^* = \begin{bmatrix} \rho v \\ \rho u v \\ p + \rho v^2 \\ \rho v w \\ (e+p)v \end{bmatrix}$$

$$G^* = 1/r \begin{bmatrix} \rho w \\ \rho u w \\ \rho v w \\ p + \rho w^2 \\ (e+p)w \end{bmatrix}, H^* = 1/r \begin{bmatrix} \rho v \\ \rho u v \\ \rho(v^2 - w^2) \\ 2\rho v w \\ (e+p)v \end{bmatrix}$$

$$\mu_\zeta = \begin{cases} \dfrac{\zeta_{max}\sinh\beta C}{\zeta_c \beta \{ 1 + [\,(\zeta/\zeta_c - 1)\sinh\beta C]^2 \}^{1/2}} & \beta > 0 \\[1.5em] 1 & \beta = 0 \end{cases}$$

$$\mu_{\zeta_\mu} = \begin{cases} \dfrac{-(\zeta/\zeta_c - 1)\sinh^2\beta C}{\zeta_c \{ 1 + [\,(\zeta/\zeta_c - 1)\sinh\beta C]^2 \}} & \beta > 0 \\[1.5em] 0 & \beta = 0 \end{cases}$$

$$\zeta_t = -(\dot{z}_m + \zeta)/t \qquad\qquad \zeta_{t\zeta} = 1/\tau$$

$$\zeta_z = 1/t \qquad\qquad\qquad\quad \zeta_{z\zeta} = 0$$

$$\zeta_r = (\cos\phi\tan\lambda)/t \qquad\quad \zeta_{r\zeta} = 0$$

$$\zeta_\phi = -r(\sin\phi\tan\lambda)/t \qquad \zeta_{\phi\zeta} = \text{Num}\ddagger$$

$$\eta_t = -\eta r_{obt}/(r_{ob} - r_b) \qquad \eta_{t\eta} = \text{Num}\ddagger$$

$$\eta_z = [\,-r_{bz} - \eta(r_{obz} - r_{bz})\,]/(r_{ob} - r_b) \qquad \eta_{z\eta} = \text{Num}\ddagger$$

$$\eta_r = 1/(r_{ob} - r_b) \qquad\qquad \eta_{r\eta} = \text{Num}\ddagger$$

$$\eta_\phi = -\eta r_{ob\phi}/(r_{ob} - r_b) \qquad \eta_{\phi\eta} = \text{Num}\ddagger$$

The calculation of the partial derivatives of r_{ob} are discussed in Sec. III.

In Eq. (2), p represents the pressure; ρ, the density; u, v, and w, the velocity components in the z, r, and ϕ directions; and e, the total energy per unit volume. The pressure, density, and velocity are related to the energy for an ideal gas by the following equation:

$$e = p/(\gamma - 1) + \rho(u^2 + v^2 + w^2)/2 \tag{3}$$

The transformed, time-dependent Euler equations are hyperbolic with respect to τ and can be solved in an iterative fashion (e.g., at $\tau = 1.0$) using an explicit, finite-difference scheme. Because of the self-similar transformation, the U_τ term in Eq. (2) approaches zero as the integration proceeds with respect to τ and results in a converged solution for large τ or after a large number of iterations at $\tau = 1.0$.

---

‡Num implies that the partial derivative must be obtained numerically since the function $r_{ob}(t, z, \phi)$ is not known analytically.
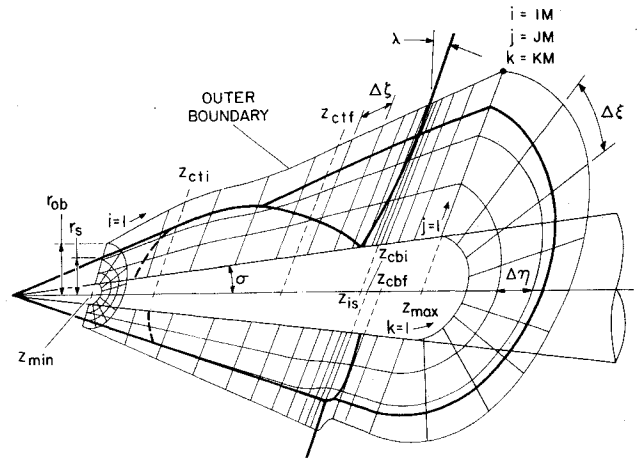

Fig. 3 Computational volume.

III. Boundary and Initial Conditions

The transformation given by Eq. (1) results in the computational grid shown in Fig. 3. At the extremities of this computational volume, the correct boundary conditions must be applied. On the surface of the cone, the tangency condition is satisfied by using an Euler predictor/modified Euler corrector with one-sided differences in the η-direction and imposing the condition $v = u \tan \sigma$ after the corrector. Since the numerical technique is iterative with respect to the independent variable of integration, and we are only interested in the converged solution and not the transient, the body boundary condition is accurately simulated[9,25,27] by following this procedure. At the 0° and 180° planes of symmetry, the "reflection principle" is applied using the conservative variables. Rather than use of image planes to implement this boundary condition, the finite-difference scheme is modified (discussed briefly in Sec. IV).

It is important to ensure that the permeable boundaries of the computational volume be hyperbolic,[25] i.e., the flow through these boundaries must be supersonic with respect to the self-similar coordinates. If this condition is satisfied, and the flow variables along such boundaries are known, then the associated grid points can be initialized using the known flow quantities and held fixed during the entire integration procedure. For the three-dimensional problem, this required that z_{min} (the distance along the z axis to the intersection of the left-hand boundary plane at $t = 1$) lie to the left of the sonic line, that z_{max} lie to the right of the incident shock, and that the outer boundary encompass the peripheral shock structure (Fig. 3). The position of z_{min}, z_{max}, and the outer boundary depend on the conical flow at the end planes.

To determine the flow at the right- and left-hand boundaries (regions 2 and 4, respectively, in Fig. 2), an existing three-dimensional, supersonic flowfield code[28] (TDSCT) was employed. Given the vehicle Mach number M_v, angle of attack α, cone half-angle σ, and ratio of specific heats γ, the TDSCT program, which treats the bow shock as a sharp discontinuity, is used to generate the conical flowfield at the right-hand boundary. In addition, given the incident shock Mach number M_i and its inclination λ, the conditions behind the incident shock or the new freestream conditions M_3 and α_3 can easily be found using the normal shock relations:

$$q_{i1} = M_i a_i \quad \text{velocity of incident shock with respect}$$
$$\text{to still air} \tag{4a}$$

$$q_{i2} = q_{i1}\{1 - [\,(\gamma - 1)M_i^2 + 2]/[\,(\gamma + 1)M_i^2\,]\}$$
$$\text{velocity of air behind incident shock with}$$
$$\text{respect to still air} \tag{4b}$$

$$p_3 = p_1[\,2\gamma M_i^2 - (\gamma - 1)\,]/(\gamma + 1) \tag{4c}$$

Table 1   Cartesian velocity components (see Fig. 2) of regions 1 and 3, and the incident shock with respect to the cone $q_j = u_j \hat{i}_x + w_j \hat{i}_z$)

j	u_j	w_j
1	$q_1 \sin \alpha$	$q_1 \cos \alpha$
3	$q_1 \sin \alpha - q_{i2} \sin \lambda$	$q_1 \cos \alpha + q_{i2} \cos \lambda$
is	$q_1 \sin \alpha - q_{i1} \sin \lambda$	$q_1 \cos \alpha + q_{i1} \cos \lambda$

$$p_3 = \rho_1 (\gamma + 1) M_i^2 / [(\gamma - 1) M_i^2 + 2] \tag{4d}$$

$$a_3 = (\gamma p_3 / \rho_3)^{1/2} \tag{4e}$$

The velocity of the gas in region 3, which is a function of the velocity in region 1, is given in Table 1. The Mach number and flow direction are given by $M_3 = q_3 / a_3$, $\alpha_3 = \tan^{-1} (u_3 / w_3)$. These conditions are then used by the TDSCT code to generate the conical flowfield at the left-hand boundary.

For the positive values of λ considered, z_{min} (which must lie to the left of the sonic line) is determined by the flow at the body in the 180° plane, and its location can be found from

$$z_{min} < (q_{4b} - a_{4b})(1 - \tan \sigma \tan \lambda) \cos \sigma \tag{5}$$

where q_{4b} is the velocity and a_{4b} is the speed of sound at the body in that plane. The location of z_{max} depends on the position of the incident shock at time $t = 1$. The distance z_{is} (Fig. 3) is given by

$$z_{is} = q_{is} \cos \kappa / \cos \lambda \tag{6}$$

where q_{is} is given in Table 1 and $\kappa = \lambda + \tan^{-1}(u_{is} / w_{is})$. Since z_{is} is known, z_{max} is selected to ensure that there is a sufficient number of longitudinal grid points to capture the Mach stem in the 0° plane.

The data describing the two conical-flow solutions generated by the TDSCT program, in addition to the state variables, include the shock position r_s and the two shock slopes $\partial r_s / \partial z$ and $\partial r_s / \partial \phi$, which are used in defining the outer boundary. The position of the outer boundary near the end planes is chosen so that in both the meridional and longitudinal directions there is an equal number of grid points between the conical bow shocks and it, thus imposing a condition that $r_{ob_\phi} / r_{ob} = r_{s_\phi} / r_s$.

In the longitudinal direction, the outer boundary is composed of conical rays from the vertex near the end planes and cubic polynomials in between (Fig. 3). In the 0° plane, for example, the outer boundary is composed of a conical ray that extends from z_{min} to z_{cbi}, followed by a cubic polynomial to z_{cbf}, and finally another conical ray to z_{max}. At z_{cbi} and z_{cbf}, both r_{ob} and r_{ob_z} are continuous. Only the four constants z_{cbi} and z_{cbf} for the 0° plane and z_{cti} and z_{ctf} for the 180° plane need to be specified. A simple linear interpolation between the bottom and top values is used for the analogous parameters in the remaining meridional planes. In most of the examples presented later, z_{ctf} and z_{cbi} were set equal to z_{is} based on the shock patterns of previously computed test cases.

Equation (2) requires that r_{ob_t}, r_{ob_z}, and r_{ob_ϕ} be known. For the conical portion of the outer boundary, these functions are easily determined from the known shape of the conical bow shocks ($r_{ob_t} = 0$). However, it is slightly more difficult to determine these functions for the nonconical portion.

In a given meridional plane, the cubic can be written as

$$f(\zeta) = a + b(\zeta - \zeta_1) + c(\zeta - \zeta_1)^2 + d(\zeta - \zeta_1)^3 \tag{7}$$

where

$\zeta_1 =$ value for ζ for z_{ci}, $\zeta_2 =$ value for ζ for z_{cf}

$$[\text{e.g.}, z_{ci} = z_{cti}(\phi / \pi) + (1 - (\phi / \pi)z_{cbi}]$$

and

$$a = r_{ob_1} / t, \quad b = r_{ob_{z_1}} / (1 + r_{ob_{z_1}})$$

$$\cos \phi \tan \lambda) = f_{\zeta_1}$$

$$x = [r_{ob_2} / t - r_{ob_1} / t - (\zeta_2 - \zeta_1)b] / (\zeta_2 - \zeta_1)^2,$$

$$y = (f_{\zeta_2} - f_{\zeta_1}) / 2(\zeta_2 - \zeta_1)$$

$$d = 2(y - x) / (\zeta_2 - \zeta_1), \quad c = x - d(\zeta_2 - \zeta_1)$$

The quantities r_{ob_t} and r_{ob_z} are given by

$$r_{ob_t} = (f + tf_\zeta \zeta_z / (1 - tf_\zeta \zeta_r) \tag{8}$$

and

$$r_{ob_z} = tf_\zeta \zeta_z / (1 - tf_\zeta \zeta_r) \tag{9}$$

where $f_\zeta = \partial f / \partial \zeta$ and ζ_t, ζ_z, and ζ_r are given in Eq. (2).

Since the circumferential variation of the quantities a, b, c, and d in Eq. (7) is not known, r_{ob_ϕ} must be computed numerically. This is easily accomplished using the following expression and noting that r_{ob_ϕ} is zero at the planes of symmetry

$$r_{ob_\phi} = r_{ob_\xi} - r_{ob_z} \partial z / \partial \xi \tag{10}$$

In Eqs. (10), r_{ob_ξ} and $\partial z / \partial \xi$ are numerically using a second-order, central-difference formula.

With the computational volume established and the geometrical derivatives defined, the flow variables at the nodes can be initialized. Grid points that fall in region 1, i.e., between the original bow shock and the incident shock, are assigned values equal to the original freestream. For the cases considered here, p_1 and ρ_1 are set equal to 1.0, which implies that $q_1 = M_v \sqrt{\gamma}$. The individual velocity components for region 1 as a function of α and ϕ are given in Table 2. The conditions in region 3, i.e., behind the incident shock and above the new bow shock, are given by Eq. (4), while the velocity components of q_3 are also presented in Table 2. Between z_{is} and z_{max}, and below the original bow shock, the right-side conical-flow values (region 2) are assigned, while between z_{min} and z_{is}, and below the new bow shock, the left-side conical-flow values (region 4) are assigned.

To initiate the calculation, the integration stepsize $\Delta \tau$ must be specified. If we use a one-dimensional, amplification matrix, stability analysis[25,29] a governing stepsize for $\Delta \tau$ relative to the μ, η, and ξ directions can be found as follows

$$\Delta \tau_\mu = CN \Delta \zeta / \mu_\zeta |\zeta_t + u \zeta_z + v \zeta_r + (w / r) \zeta_\phi$$

$$\pm a [\zeta_z^2 + \zeta_r^2 + (\zeta_\phi / r)^2]^{1/2} |_{max} \tag{11a}$$

$$\Delta \tau_\eta = CN \Delta \eta / |\eta_t + u \eta_z + v \eta_r + (w / r) \eta_\phi$$

$$\pm a [\eta_z^2 + \eta_r^2 + (\eta_\phi / r)^2]^{1/2} |_{max} \tag{11b}$$

$$\Delta \tau_\xi = CN \Delta \xi / |w \pm a|_{max} \tag{11c}$$

where CN is the Courant number and is usually set equal to

Table 2   Cylindrical velocity components of regions 1 and 3 with respect to the cone ($q_j = u_j \hat{i}_z + v_j \hat{i}_r + w_j \hat{i}_\phi$)

j	u_j	v_j	w_j
1	$q_1 \cos \alpha$	$-q_1 \sin \alpha \cos \phi$	$q_1 \sin \alpha \sin \phi$
3	$q_3 \cos \alpha_3$	$-q_3 \sin \alpha_3 \cos \phi$	$q_3 \sin \alpha_3 \sin \phi$

1.0. For the calculation to be stable, the minimum of the step-sizes in Eqs. (11) is used

$$\Delta\tau = \min(\Delta\tau_\mu, \Delta\tau_\eta, \Delta\tau_\xi) \tag{12}$$

During a typical calculation, $\Delta\tau$ is recomputed every 50 iterations, and it is generally Eq. (11b) evaluated at the outer boundary in the left-hand end-plane for $\phi = 180°$ that governs the stepsize.

IV. Finite-Difference Algorithm

Equation (2) is solved iteratively at time $\tau = 1.0$ using the second-order, noncentered, finite-difference scheme devised by MacCormack.[30] It has been demonstrated[9,27,31,32] that this scheme can accurately determine the correct strength and location of all discontinuities in the flow as well as the continuous regions. The version of MacCormack's scheme used here as applied to Eq. (2) is

$$U_{i,j,k}^{(1)} = U_{i,j,k}^n - \frac{\Delta\tau}{\Delta\mu}(E_{i+1,j,k}^n - E_{i,j,k}^n)$$

$$- \frac{\Delta\tau}{\Delta\eta}(F_{i,j+1,k}^n - F_{i,j,k}^n)$$

$$- \frac{\Delta\tau}{\Delta\xi}(G_{i,j,k+1}^n - G_{i,j,k}^n) - \Delta\tau H_{i,j,k}^n \tag{13a}$$

$$U_{i,j,k}^{n+1} = \tfrac{1}{2}[U_{i,j,k}^n + U_{i,j,k}^{(1)} - \frac{\Delta\tau}{\Delta\mu}(E_{i,j,k}^{(1)}$$

$$- E_{i-1,j,k}^{(1)}) - \frac{\Delta\tau}{\Delta\eta}(F_{i,j,k}^{(1)} - F_{i,j-1,k}^{(1)})$$

$$- \frac{\Delta\tau}{\Delta\xi}(G_{i,j,k}^{(1)} - G_{i,j,k-1}^{(1)}) - \Delta\tau H_{i,j,k}^{(1)} + D_{i,j,k}^n] \tag{13b}$$

where

$$U_{i,j,k}^n = U(n\Delta\tau, i\Delta\mu, j\Delta\eta, k\Delta\xi)$$

$$E_{i,j,k}^n = E(U_{i,j,k}^n, n\Delta\tau, i\Delta\mu, j\Delta\eta, k\Delta\xi)$$

$$E_{i,j,k}^{(1)} = E[U_{i,j,k}^{(1)}, (n+1)\Delta\tau, i\Delta\mu, j\Delta\eta, k\Delta\eta], \text{etc.}$$

The term $D_{i,j,k}^n$ is a fourth-order smoothing term in the μ and η directions (which does not affect the accuracy of the algorithm) and is given by

$$D_{i,j,k}^n = -d_\mu[U_{i+2,j,k}^n + U_{i-2,j,k}^n$$

$$-4(U_{i+1,j,k}^n + U_{i-1,j,k}^n) + 6U_{i,j,k}^n] - d_\eta[U_{i,j+2,k}^n + U_{I,J-2,k}^N$$

$$-4(U_{i,j+1,k}^n + U_{i,j-1,k}^n) + 6U_{i,j,k}^n] \tag{13c}$$

where d_μ and d_η are constants that control the degree of smoothing. The intervals $\Delta\mu$, $\Delta\eta$, and $\Delta\xi$ depend on the number of grid points selected in each direction, and the integration stepsize $\Delta\tau$ is defined in Eq. (12).

At the planes of symmetry, special differences for the G_ξ term of Eq. (2) are required to apply the reflection principle since an image plane is not used. The terms G_1, G_2, G_3, and G_5 in Eq. (2) are odd functions with respect to the planes of symmetry while G_4 is an even function. In the predictor Eq. (13a) at $\phi = 180($ ($k = $KM in Fig. 3), the forward difference of G_ξ therefore, is replaced by

$$G_\xi = -(\Delta\tau/\Delta\xi)(G_{i,j,\text{KM}-1}^n + G_{i,j,\text{KM}}^n)$$

for G_1, G_2, G_3, and G_5

and

$$G_\xi = (\Delta\tau/\Delta\xi)(G_{i,j,\text{KM}-1}^n - G_{i,j,\text{KM}}^n) \text{ for } G_4$$

In the corrector Eq. (13b) at $\phi = 0°$ ($k = 1$), the backward difference of G_ξ is replaced by

$$G_\xi = (\Delta\tau/\Delta\xi)(G_{i,j,2}^{(1)} + G_{i,j,1}^{(1)})$$

for G_1, G_2, G_3, and G_5

and

$$G_\xi = (\Delta\tau/\Delta\xi)(G_{i,j,1}^{(1)} - G_{i,j,2}^{(1)}) \text{ for } G_4$$

The geometric derivatives that are set equal to Num in Eq. (2) must be evaluated numerically for reasons explained earlier. To do this, the following second-order, finite-difference formula is used

$$\partial A/\partial x = (\epsilon_1 A_{i+1} + \epsilon_2 A_i + \epsilon_3 A_{i-1})/2\Delta x \tag{14}$$

where

$\epsilon_1 = -3, \epsilon_2 = 4, \epsilon_3 = -1$, forward one-sided difference

$\epsilon_1 = 1, \epsilon_2 = 0, \epsilon_3 = -1$, central difference

$\epsilon_1 = 3, \epsilon_2 = -4, \epsilon_3 = 1$, backward one-sided difference

V. Numerical Results

The computational grid for a typical TDSOS case consisted of $46 \times 30 \times 10$ points in the μ, η, ξ directions, and required 500 iterations to obtain a converged solution. The vector arithmetic capability of the CDC 7600 enabled solutions to be computed in 18 min.

The results generated by the TDSOS computer code yield data that describe the entire flowfield. However, the distribution of the surface-flow variables in the vicinity of the impinging shock (or where the peak pressure occurs) contain minor oscillations characteristic of the shock-capturing technique. Thus, to improve the prediction of the peak surface pressure and at the same time check the TDSOS numerical results, a simple analytic procedure was developed to calculate the local flow at the transmitted shock impingement points. This supplemental calculation is performed in both the leeward plane ($\phi = 0°$), where, for the encounter angles considered, only Mach reflection can occur, and the windward plane, where either regular or Mach reflection of the transmitted incident shock can occur.

The shock impingement points $(z/t)_i$ labeled R and M in Fig. 4 are determined from the numerical solution. The
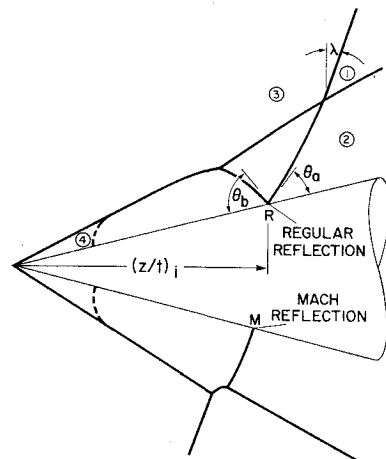

Fig. 4 Analytic calculation for regular or Mach reflection of transmitted incident shock at the body.

velocity of the impingement point with respect to the surface of the cone is then given by

$$q_i = (z/t)_i/\cos \sigma$$

Knowing this velocity, the right-side conical-flow solution (region 2), and whether a Mach or regular reflection occurs (which can be determined for the most part from flowfield contour plots), one can determine the postimpingement flow.

For Mach reflection, the Rankine-Hugoniot relations for a normal shock are applied to obtain the postimpingement-flow variables easily. For regular reflection, the inclination of the transmitted shock θ_a in Fig. 4 is required and can be measured from the computer-generated contour plots. In combination with the regular shock reflection relations, it is used to determine the flow behind and the inclination θ_b of the reflected transmitted shock.

To verify the TDSOS numerical procedure, one of the head-on encounters experimentally tested by Merritt and Aronson[20] was modeled, namely, $M_v = 3.10$ and $M_i = 1.29$. The uniform preblast and postblast conditions required to generate the conical-flow, end-plane solutions are given in Table 3. In Fig. 5, the numerical results in the form of a pressure contour plot are superimposed on a schlieren photograph of the model during its flight. The agreement of the computed and observed shock structure is very good. An advantage of the numerical solution is that it can focus on the flow in a given meridional plane, whereas the experiment that includes both background and foreground flow cannot. Thus, the structure of the experimentally transmitted incident shock in Fig. 5 is lost, but can be observed from the numerical solution.

Table 3   Uniform-flow conditions in regions 1 and 3 for computational cases

$M_v = M_I$	α_I	σ	M_i	λ	M_3	α_3
3.10	0.0	9.0	1.39	0.0	3.27484	0.0
3.10	0.0	9.0	1.61	0.0	3.32252	0.0
3.12	0.0	9.0	2.07	0.0	3.36277	0.0
5.00	0.0	11.2	1.23	0.0	4.99344	0.0
				10.0	4.98882	−0.64850
				19.0	4.97685	−1.21885
				22.0	4.97125	−1.40404
				24.0	4.96709	−1.52577
				32.0	4.94703	−1.99609
				40.0	4.92180	−2.43389

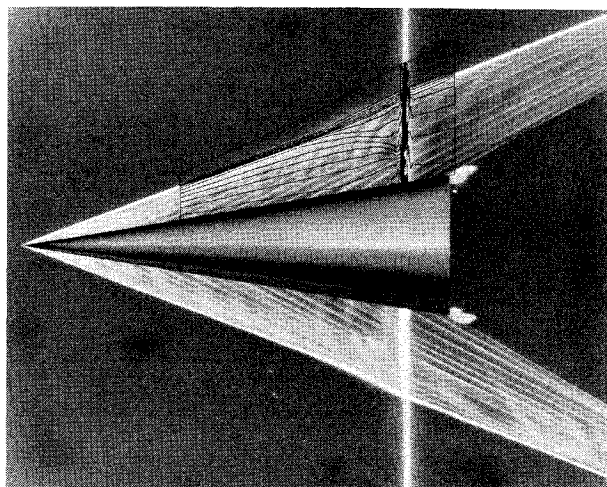**Fig. 5   Comparison of numerical solution with experiment for head-on encounter,** $M_v = 3.1$, $\alpha = 0°$, $\sigma = 9°$, $M_i = 1.39$, $\lambda = 0°$.
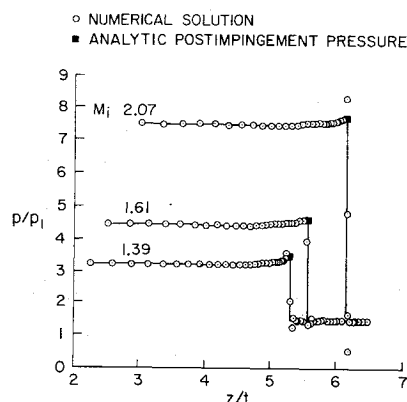
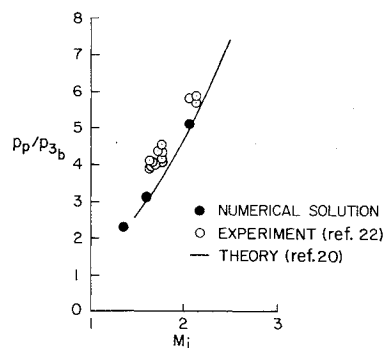**Fig. 6   Surface pressure distribution for head-on encounters;** $M_v = 3.1$, $\alpha = 0°$, $\sigma = 9°$, $\lambda = 0°$.

Fig. 7   Variation of peak surface pressure with incident shock Mach number for head-on encounters; $M_v = 3.1$, $\alpha = 0°$, $\sigma = 9°$, $\lambda = 0°$.

The surface pressure distribution for the numerical solution of this case and two others (see Table 3) for which experiments have been performed[22] is shown in Fig. 6. The numerical data points are plotted to indicate the degree of clustering used and the amplitude of the postcursor and precursor oscillations associated with the SCT. All three cases resulted in a Mach reflection of the transmitted incident shock, and the analytically determined postimpingement pressures or, in this case, peak pressures are shown and agree well with the numerical data.

A comparison of the peak surface pressures determined from the TDSOS code, experiment,[21] and an approximate theory[20] is shown in Fig. 7. The approximate theory assumes that the axial location of the impingement point of the transmitted shock is the same as that of the intersection of the incident shock and original bow shock. This information is then used in conjunction with the normal shock relations to calculate the peak pressure. The agreement, as shown in Fig. 7, between this theory and the TDSOS results, is good mainly because the approximate theory's underlying assumption regarding the impingement point location is very good.

The latest experiment[24] to be performed on this problem involved an 11.2° half-angle cone traveling at Mach 5 and was to have been struck by a Mach 1.23 ($p_3/p_1 = 1.6$) incident shock at encounter angles near the critical angle, which results in transition from Mach to regular reflection of the transmitted shock. An effort was made to predict some of the flowfields prior to the actual experiment, and, toward this end, several numerical solutions were obtained. The specific encounter angles, including the postblast, uniform-flow conditions, are given in Table 3.

A sequence of density contour plots typical of the solutions obtained is shown in Fig. 8 for the $\lambda = 24°$ encounter. The coalescence of constant-density lines, indicative of a discontinuity, depicts a wave pattern in the $\phi = 0°$ plane similar to that obtained for the internal-corner-flow problem,[27] i.e., the
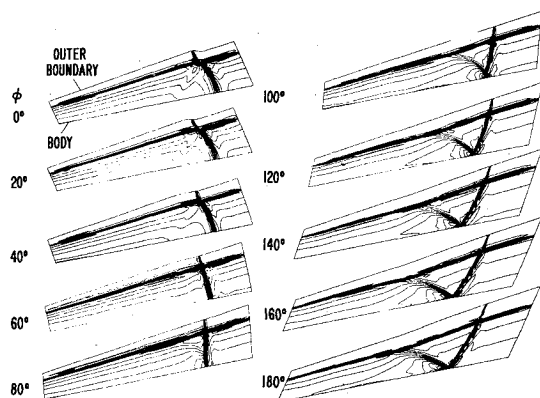
Fig. 8 Density contours in all meridional computational planes for an oblique encounter; $M_v = 5.0$, $\alpha = 0°$, $\sigma = 11.2°$, $M_i = 1.23$, $\lambda = 24°$.
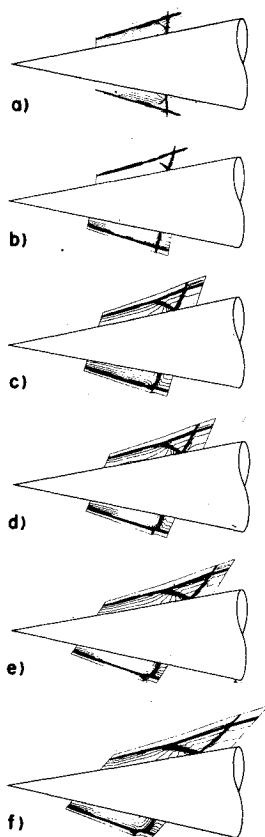

Fig. 9 Pressure contours of windward and leeward computational planes for oblique encounters; $M_v = 5.0$, $\alpha = 0°$, $\sigma = 11.2°$, $M_i = 1.23$. a) $\lambda = 0°$, b) $\lambda = 10°$, c) $\lambda = 19°$, d) $\lambda = 22°$, e) $\lambda = 32°$, f) $\lambda = 40°$.
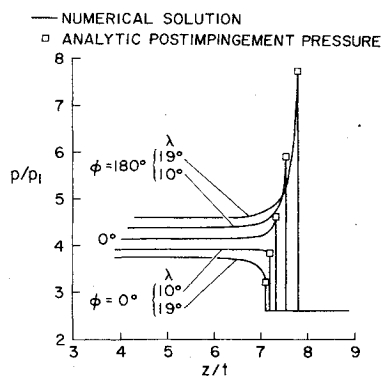

Fig. 10 Surface pressure distribution in leeward ($\phi = 0°$) and windward ($\phi = 180°$) planes (Mach reflection); $M_v = 5$, $\alpha = 0°$, $\sigma = 11.2°$, $M_i = 1.23056$ ($p_3/p_1 = 1.6$), $t = 1.0$.
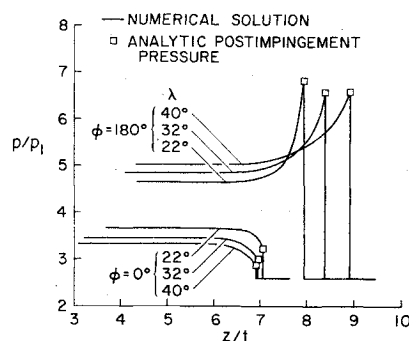

Fig. 11 Surface pressure distribution in leeward ($\phi = 0°$) and windward ($\phi = 180°$) planes (Regular reflection); $M_v = 5$, $\alpha = 0°$, $\sigma = 11.2°$, $M_i = 1.23056$ ($p_3/p_1 = 1.6$), $t = 1.0$.

Table 4 Peak surface pressure: $M_v = 5$, $\alpha = 0°$, $\sigma = 11.2°$, and $M_i = 1.230563$; $\phi = 180°$, $t = 1.0$

λ	p_p/p_1	$(z/t)i$	θ_a	θ_b	M_b
Mach reflection					
0.0	4.61	7.337	....	....	....
10.0	5.91	7.546	....	....	....
19.0	7.72	7.806	....	....	....
Regular reflection					
22.0	6.85	7.913	45.3	54.3	0.99758
24.0	6.66	7.999	43.5	48.2	1.10434
32.0	6.57	8.398	36.5	34.8	1.45522
40.0	6.55	8.929	30.0	26.4	1.87248

existence of two triple points joined by a corner shock (also equivalent to the single tangent model of Smyrl[1]). Emanating from both triple points are slip surfaces, shown as a weak coalescence of lines, that eventually strike the body. The transmitted incident shock is curved (concave with respect to the vertex of the cone) due to the gradients in the radial direction and strikes the body perpendicularly. The flow in the region downstream of the transmitted shock is compressed and, therefore, the peak pressure in this plane does not occur directly behind the shock but farther downstream. In the $\phi = 80°$ plane, the transmitted shock becomes convex, and compression waves begin to originate from the most curved region of the shock. With increasing ϕ, these compression waves coalesce and result in a "λ-shock" formation. As ϕ increases further, the small Mach stem of the λ-shock disappears and the transmitted incident shock reflects regularly from the surface of the cone.

Pressure contours of the flow in the windward and leeward planes for the remaining encounter angles are shown in Fig. 9. For $\lambda = 0°$, $10°$, and $19°$, Mach reflection of the transmitted shock in the windward plane occurs, while for $\lambda = 22°$, $24°$,

$32°$, and $40°$, regular reflection occurs. Using only the contour plots and for encounter angles near transition, it is difficult to determine whether Mach or regular reflection occurs. But in combination with the analytic technique described at the beginning of Sec. V, the guesswork is minimized.

Plots of the surface pressure distribution in the $0°$ and $180°$ planes are shown in Fig. 10 for Mach reflection and in Fig. 11 for regular reflection. The individual points are not plotted, but the degree of clustering (see Fig. 6) is the same for all cases ($\beta = 5$). The postimpingement pressures calculated from the analytic technique described earlier faired in nicely with the numerical data, and the peak pressures in the windward plane are summarized in Table 4. Note that the peak pressure in the leeward plane does not occur directly behind the impinging shock wave, but is actually equal to the quasi-steady conical value. For the Mach reflection cases, the pressure spike is much thinner than for the regular reflection cases (compare Figs. 10 and 11).
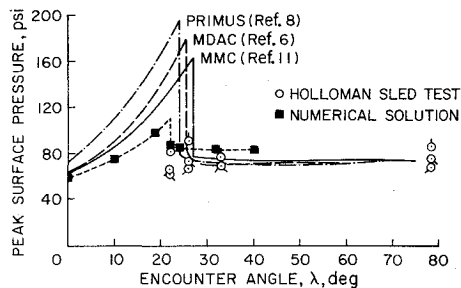
Fig. 12　Variation of peak surface pressure with encounter angle; $M_v = 5$, $\alpha = 0°$, $\sigma = 11.2°$, $M_i = 1.23056$ ($p_3/p_1 = 1.6$), $h = 4500$ ft, $t = 1.0$.

A comparison of the numerically predicted peak pressure as a function of the encounter angle λ with three approximate theories [1) PRIMUS[8]-Picatinny Arsenal, 2) MDAC[6] McDonnell Douglas Astronautics Co., and 3) MMC[12]-Martin Marietta Corp.] and experimental data[23,24] is shown in Fig. 12. All three theories grossly over-predict the maximum peak surface pressure compared to the numerical results and the experimental data. The encounter angle for transition from Mach to regular reflection of the transmitted incident shock is different for each solution and it is difficult to determine from the experimental data what the correct value of λ should be. Both the first[23] and second[24] series of Holloman sled test data are shown in this figure and appear to fall in the regular reflection regime (based on the numerical results). The three points plotted for each encounter angle represent pressure data from probes at three different axial locations. The discrepancies between the numerical and experimental data can most likely be attributed to the 10 μsec rise time of the transducer/data recording system, which would tend to truncate the numerically obtained pressure spikes.

VI.　Conclusions

The procedure developed to model the three-dimensional, unsteady, shock-on-shock problem accurately predicts the complicated interactive flowfield, including the structure of the resulting shock pattern and the variation of the surface-flow variables. The results obtained verify the early models for the shock structure suggested by Smyrl,[1] as did later experiments. Predicted values of the peak pressure in the windward plane for various encounter angles agree fairly well with existing experimental results and, in conjunction with the remaining flowfield data, should provide the vehicle designer with an abundance of information. Finally, it is believed that, based on the results of these numerical solutions and the latest experimental data, the concern originally generated by the large peak pressures predicted by approximate techniques is somewhat unwarranted.

References

[1] Smyrl, J.l., "The Impact of a Shock-Wave on a Thin Two-Dimensional Aerofoil Moving at Supersonic Speed," *Journal of Fluid Mechanics*, Vol. 15, Feb. 1963, pp. 223-240.

[2] Miles, J.W., "A Note on Shock-Shock Diffraction," *Journal of Fluid Mechanics*, Vol. 22, May 1965, pp. 95-102.

[3] Blankenship, V.D., "Shock-Shock Interaction on a Slender Supersonic Cone," *Journal of Fluid Mechanics*, Vol. 22, July 1965, pp. 599-615.

[4] Inger, G.R., "Blast Wave Impingement on a Slender Wedge Moving at Hypersonic Speeds," *AIAA Journal*, Vol. 4, March 1966, pp. 428-435.

[5] Inger, G.R., "Oblique Blast Impingement on Slender Hypersonic Bodies," *AIAA Journal*, Vol. 4, Aug. 1966, pp. 1475-1477.

[6] Gardiner, C.P., "Shock-On-Shock Interaction," MDAC memorandum A3-830-BBB1-72-53, Aug. 1972, McDonnell Douglas Astronautics Corp., Huntington Beach, Calif.

[7] Hayes, W., "Approximations for Shock-Shock Interctions at Near Normal Incidence," Aeronautical Research Associates of Princeton, Inc. Working Paper No. 72-18, Jan. 1973, Princeton, N.J.

[8] Hudgins, H.E. Jr. and Friedman, E.M., "Shock-Shock Interaction Studies for Weak Incident Shocks," Picatinny Arsenal TR-4590, Dec. 1973, Picatinny, N.J.

[9] Kutler, P., Sakell, L., and Aiello, G., "On the Shock-on-Shock Interaction Problem," *AIAA Journal*, Vol. 13, March 1975, pp. 361-367.

[10] Miller, W.D., Schindel, L., and Ruetenik, J.R., "Computer Program for the Calculation of the Interaction of a Blast Wave with a Non-uniform Shock Layer," MIT Rept. ASRL-TR-121-2, Sept. 1964, Cambridge, Mass.

[11] Aiello, G.F., "A Pretest Analysis to Support the Design of the Phase II Sled Test Program," Martin Marietta ANA 10721000-006, March 1974, Martin Marietta Corp., Orlando, Fla.

[12] McNamara, W., "FLAME Computer Code for the Axisymmetric Interaction of a Blast Wave with a Shock Layer on a Blunt Body," *Journal of Spacecraft and Rockets*, Vol. 4, June 1967, pp. 790-795.

[13] Hudgins, H.E., Jr. and Freedman, E.M., "Shock-on-Shock Interaction Studies for Weak Incident Shocks," Feltman Research Labs, Picatinny Arsenal, TR-4590, Dec. 1973, Picatinny, N.J.

[14] Culotta,A., "Method of Characteristics Numerical Simulation of Unsteady Tunnel Flows with Reflections," Martin Marietta Aerospace, Orlando Division, OR 10, 383, Jan. 1970, Orlando, Fla.

[15] Aiello, G.F., "The Broadside Encounter Between a Sharp Cone and a Planar Blast Wave," Martin Marietta Aerospace, Orlando Division, Document ANA 01900162-002, May 1973, Orlando, Fla.

[16] Brown, E.A. and Mullaney, G.J., "Technique for Studying the Shock-on-Shock Problem," *AIAA Journal*, Vol. 3, Nov. 1965, pp. 2167-2168.

[17] Brown, E.A. and Mullaney, G.J., "Experiments on the Head-on Shock-Shock Interaction," *AIAA Journal*, Vol. 3, Nov. 1965, pp. 2168-2170.

[18] Merritt, D.L. and Aronson, P.M., "Wind-Tunnel Simulation of Head-on Bow Wave-Blast Wave Interactions," NOLTR 67-123, Aug. 1967, Naval Ordnance Lab., White Oak, Silver Spring, Md.

[19] Baltakis, F.P., Merritt, D.L., and Aronson, P.M., "Two Techniques of Simulating the Interaction of a Supersonic Vehicle with a Blast Wave," NOLTR 67-154, Oct. 1967, Naval Ordnance Lab., White Oak, Silver Spring, Md.

[20] Merritt, D.L. and Aronson, P.M., "Experimental Studies of Shock-Shock Interactins on a 9° Cone," NOLTR 67-182, Jan. 1968, Naval Ordnance Lab., White Oak, Silver Spring, Md.

[21] Merritt, D.L. and Arsonson, P.M., "Oblique Shock Interaction Experiments," NOLTR 69-108, May 1969, Naval Ordnance Lab., White Oak, Silver Spring, Md.

[22] Baltakis, F.P., "Shock Interaction Surface Pressures for Hemispherical and Conical Bodies," NOLTR 71-27, Feb. 1971, Naval Ordnance Lab., White Oak, Silver Springs, Md.

[23] Rutenik, J.R., Cole, E.L., and Jones, R.E., "Shock-On-Shock Pressure Measurements at Mach 5 from Rocket-Propelled Sled Tests, Phase I: Lateral Intercepts," KAMAN AviDyne Rept. KA TR-98, Aug. 1973, KAMAN Sciences Corp., Burlington, Mass.

[24] Patrick, R.E., "Phase II Shock-On-Shock Experiment," Teledyne Brown Engineering, Summary Rept., for Period 1 June 1974-30 Nov. 1974, Dec. 1974, Huntsville, Ala.

[25] Kutler, P., "Computation of Thre-Dimensional, Inviscid Supersonic Flows," Lecture notes from AGARD/VKI Short Course on "Computational Methods in Fluid Dynamics," Feb. 1974; to be published by Springer-Verlag in *Lecture Notes in Physics*.

[26] Thomas, P.D., Vinokur, M., Bastianon, R., and Conti, R.J., "Numerical Solution for the Three-Dimensional Inviscid Supersonic Flow of a Blunt Delta Body," *AIAA Journal*, Vol. 10, July 1972, pp. 887-894.

[27] Kutler, P., "Supersonic Flow in the Corner Formed by Two Intersecting Wedges," *AIAA Journal*, Vol. 12, May 1974, pp. 577-578.

[28] Kutler, P., Reinhardt, W.A., and Warming, R.F., "Multishocked, Three-Dimensional Supersonic Flowfields with Real Gas Effects," *AIAA Journal*, Vol. 11, May 1973, pp. 657-664.

[29] Richtmyer, R.D., and Morton, K.W., *Difference Methods for Initial-Value Problems*, Wiley, New York, 1967, pp. 302-303.

[30] MacCormack, R.W., "The Effect of Viscosity in Hypervelocity Impace Cratering," AIAA Paper 69-354, Cincinnati, Ohio, 1969.

[31] Kutler, P. and Lomax, H., "Shock-Capturing, Finite-Difference Approach to Supersonic Flows," *Journal of Spacecraft and Rockets*, Vol. 8, Dec. 1971, pp. 1175-1182.

[32] Kutler, P., Warming, R.F., and Lomax, H., "Computation of Space Shuttle Flowfields Using Noncentered Finite-Difference Schemes," *AIAA Journal*, Vol. 11, Feb. 1973, pp. 196-204.